ISSN 1392–1320 MATERIALS SCIENCE (MEDŽIAGOTYRA). Vol. 29, No. 1. 2023

Crack Evolution and Computational Model Based Thermal Stress Evaluation of Laser Cladding of HVOF Sprayed WC/Co Deposits

Chao Yang ZHANG, Ming Der JEAN *

College of Arts and Design/Research Center of Mintai Arts/Research Center of Cross-Strait Arts and Social Science, Jimei University, 185 Yinjiang Rd., Jimei District, Xiamen,361021, China

http://dx.doi.org/10.5755/j02.ms.30876

Received 08 March 2022; accepted 25 April 2022

A comprehensive experimental study on high-velocity oxygen-fuel (HVOF)- sprayed tungsten carbide/cobalt deposits using laser cladding was conducted. Based on the principles of central composite design, a response surface methodology was elaborated. The results show that a higher thermal gradient cannot be easily generated in the cladding, the claddings had completely melted, and the structure is highly dense without microcracks. The brighter white splats indicate unmolten material. The resulting lower residual stress decreases the fracture crack activities and does not easily induce delamination in the laser clads. Experimental data indicate that the predictions of the second-order model are quite accurate, and it is a reliable predictor of the stress for laser-based HVOF coatings. Findings from this study would contribute considerably to optimizing the experiments and achieving an enhanced structural evolution in the protective coating of traditional handicraft products by laser cladding.

Keywords: tungsten cemented carbide/cobalt (WC/Co), high-velocity oxygen-fuel (HVOF), central composite design, scanning electronic microscope (SEM), residual stress behavior, traditional handicraft, laser cladding.

1. INTRODUCTION

Cermet composite coatings are used extensively in hard-facing applications in the form of coatings, which have attracted much attention owing to their superior features in the field of additive manufacturing, metallic sculpture coating, and repair in the stone-carving arts. They provide the product with the specific properties of higher hardness, strong wear resistance, and better corrosion resistance for surface modification in the case of hard metal cutting tools, biomedical implants, or traditional handicraft products [1]. Ultrahard cermet composites are proven to be excellent materials for such surface modification [2 – 4]. Recent studies on the hard-facing fabrication of composite coatings, including tungsten and its alloys, show excellent properties [5 – 7]. These are promising candidates due to their high wear or corrosion resistance and are suitable for the surface protection of metal sculptures and stone carving products where the focus is mostly on improving the surface of the products. A series of surface modification technologies have been explored to protect traditional handicraft products from wear, corrosion, and fatigue damage, and these include arc welding, thermal spraying, nitriding, sputtering, laser cladding, etc. [8 – 12]. However, thermal spray deposited coatings have drawbacks such as high porosity, high residual stresses, and poor adherence to the substrate. Laser cladding results in superior properties that were previously unachievable and has several advantages over thermal spray technologies [13 – 15]. It greatly reduces porosity and residual stresses, creates a metallurgical bond with the base material, as well as improves adhesion between the particles of the coating [16, 17]. Therefore, it has become a promising surface technology for protective coatings that can resist specific environments and has drawn more attention in the field of traditional handicraft manufacturing [18 – 21].

During laser cladding, the inevitable residual stresses induced by thermal spraying processes create misfit strain that arises from differences in the thermal expansions of the composites, thus causing cracking due to the anisotropy properties in laser cladding [22, 23]. There have been several reports on the residual strain behavior in the case of surface modifications [24 – 26]. Kapadia et al. studied the residual stress in the fracture mechanics of electron beam welding, which is twice the stress in the substrate. Experimental results showed that when the tensile stress near the crack tip is large, stress redistribution will occur, which could significantly affect subsequent crack propagation [27]. Stadelmann et al. analyzed the mechanical properties and residual stress developed when ZrB2–SiC ceramic composites are sintered by spark plasma. The thermal residual stress distribution of the three ZrB2–SiC ceramic composites have no obvious difference between the stress distributions at 200 MPa and 300 MPa [28]. Zafar & Sharma studied the flexural properties and residual stress of nanometric WC-12Co microwave cladding and found that the flexural strength of the nano WC-12Co microwave cladding was approximately 14 % higher than that of micrometric cladding and showing that the stress value of nanometric cladding layer was 68 % higher than that of micrometric cladding layer [29]. Wang et al. studied the thermal stability and work hardening of shot-peened tungsten carbide and introduced the thermal stability of residual stresses and work hardening of shot peened tungsten cemented carbide. The results showed the compressive residual stress of WC-Co clads, indicating that the shot-peened WC-Co composite has good thermal stability at 850 °C [30]. Suárez et al. described the residual stresses generated within laser clads using the synchrotron

---

*Corresponding author. Tel.: +0592-6181815; fax: +0592-6180809.
E-mail address: *201961000102@jmu.edu.cn* (M. D. Jean)

radiation diffraction and the finite element method. The results showed that the compressive residual stresses of the WC-Co composite indicate that the WC-Co composite treated by shot peening gives good thermal stability [31]. Control of residual stresses using finite element analysis in 2Si-B-3C-N with Nb joints in the Ag-Cu-Ti-Mo composite sandwich was developed by Pan et al. [32]. In summary, it was found that laser clads are anisotropic and that there are inhomogeneous solidified regions in which the residual stress behavior of the laser clads is nonlinear. Thus, conventional methods such as numerical analytical theories based on trial and error have difficulty in predicting the residual stress behavior of the laser clad deposit. To control the residual stress behavior and reliability of the laser clad made from WC/Co composites, several attempts are needed to model the residual stress behavior of the laser clad deposits [33, 34]. Recently, many methods have been developed for the optimization study in the literature and some of the reviews can be found in [35, 36]. The response surface methodology (RSM) of optimization becomes more attractive in laser clads. However, the RSM in the recent study provides an alternative approach to studying the effect of the different variables and developing potential abilities to predict the residual stress behavior of laser-clad deposits in traditional handicraft products while employing fewer experiments. Accordingly, more effort is inevitable for modeling studies on the residual stress of laser cladding in the prediction of process optimization. The RSM permits a reduction in the number of experiments as the interactions between the various parameters affecting the responses is a promising tool to establish a reliable relationship between the response and variables. RSM is widely used in industry, especially where several input variables affect multiple quality characteristics of the product. Many successful applications have been reported that can improve product performance and reduce manufacturing costs. To facilitate more efficient surface protection and repair of traditional handicraft products, the laser-based HVOF coating process may be optimized.

This study applies RSM with a central composite design to investigate and optimize the effects of three laser cladding process factors, viz., laser power, scanning speed, and stand-off distance on the residual stress behavior of laser clads. In addition, the residual stress behavior and fracture crack formation are discussed for laser-based HVOF coatings.

2. EXPERIMENTS

2.1. Materials and preparations

The fiber laser cladding equipment is illustrated schematically in Fig. 1 and is composed of an IPG LS-3000 fiber laser, six-axis robot, induction power supply, computer numerical control system, and powder feeder (HUST III).

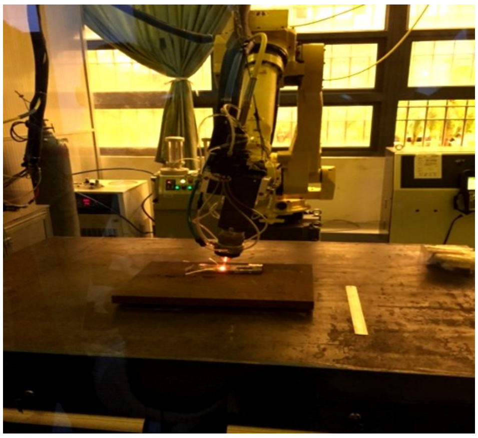

a

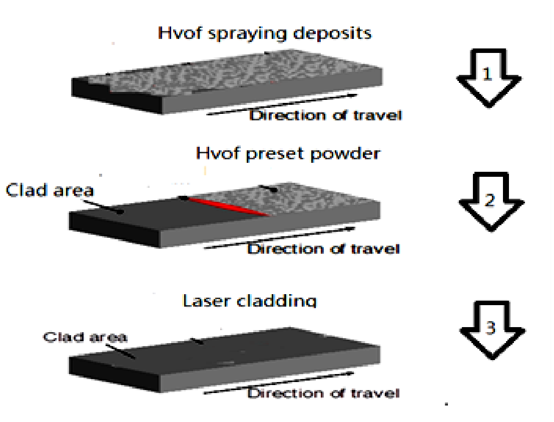

b

Fig. 1. a – the fiber laser cladding system; b – the processes of laser-based HVOF-spraying deposits

The IPG fiber laser with a maximum power of 3 KW and wavelength of 1.07 μm was adopted. An argon gas nozzle and powder feeder nozzle were projected coaxially with the laser beam through a coaxial nozzle and the laser focusing optics were mounted on the z-axis of the rotor motion system while a #45 carbon steel substrate was clamped on the x-y table. The WC–8 % CO powders were mechanically mixed, and a pre-layered coating was sprayed by HVOF. Finally, WC/Co powder was fused with a high-power coaxial laser fiber, and WC/Co powder was sprayed on the HVOF coating. The substrate was #45 steel with dimensions of 40 mm, 20 mm, and 10 mm. The working surface was cleaned with absolute ethyl alcohol. The chemical composition of the substrate metal and filler powder are shown in Table 1. WC/Co coatings were prepared by HVOF using a GTV K2 system. The spraying parameters were an oxygen flow rate of 40 l/min, the methane flow rate of 35 l/min, powder feed rate of 100 g/min, spraying distance of 20 cm, carrier gas flow rate of 24 l/min, and torch traverse speed of 27 m/min.

Table 1. Chemical composition of 45 steel

#45	Elements	C	Si	Mn	Cr	Ni	Cu Fe
steel	%	0.42 – 0.50	0.17 – 0.37	0.50 – 0.80	< 0.25	< 0.30	< 0.25 Bal.
WC/Co	Elements	WC	Co	Mo	No	Si	Ta
	%	92.1	7.8	0.02	0.025	0.02	0.035

For examining the microstructures of the composite WC/Co deposits, an OLYMPUS GX51 metallographic microscope and a Hitachi S-2600H (Tokyo, Japan) scanning electronic microscope (SEM) were used to view the samples etched by Nital for 5 – 10 sec.

In addition, residual stress analyses were carried out at the bead centerline using an x-ray diffraction (XRD) diffractometer (Proto iXRD) with the sin2ψ method. The x-ray source was a CuKα ray, $\lambda CuK\alpha$ = 1.5405 Å. The range of side angle was from ψ = -30° to ψ = 30° scanned along two different axes. The table with the control factors and levels in coded values for factors in this study is presented in Table 3, including a laser power of 1 – 3 kW, 30 – 45 mm stand-off distance, argon gas at 10 L/min, a feed rate of 15 g/min, and a scanning speed of 7 – 12 mm/sec, which was deposited onto the coatings and rapidly solidified to form a clad bead that was metallurgically bonded to the high-velocity oxygen fuel coatings.

2.2. Residual stress analysis

The surface residual stresses in the WC/Co coatings were evaluated based on the elastic deformation of polycrystalline material using the standard sin 2ψ method, whereby the stresses due to the stress concentrations cause changes in the lattice spacing. surface residual stresses in the WC/Co coatings were evaluated based on the elastic deformation of the polycrystalline material using the standard sin2ψ method, whereby the stresses due to the stress concentrations cause change in the lattice spacing. That is, the physical properties of the clads are different from those of the matrix, such as melting point, thermal expansion coefficient, elastic modulus, and Poisson's ratio [22].

The strain was measured by altering the tilt of the specimen within the diffractometer, and the residual stress (σ) was calculated by computing the slope of the linear plot (∂(2θ_ψ)/∂(sin^2 ψ)) between the d-spacing and sin2ψ. That is, the strain vs. sin2ψ is described using a linear regression function and the residual stress can be determined by the slope. Thus, residual stress can be easily induced in the clads, which can be computed as [23]:

$$\sigma = -\frac{E}{2(1+\mu)}\cot(\theta_0)\frac{\partial(2\theta_{\psi})}{\partial(sin^2\psi)}\frac{\pi}{180} \ , \qquad (1)$$

where σ is the residual stress of the laser clads; E and v are Young's modulus and Poisson's ratio of the laser clads, respectively. θ_0 and θ_ψ are the unstressed and stressed diffraction angles, respectively, and ψ is the tilt angle. To ensure the repeatability of residual stress values, three samples were tested for each laser clad. In the sin2ψ method, the R^2 value of the regression function and the range of the residual stress within one standard deviation of the average are determined. Owing to the thermal effect, residual stresses can be easily induced along with crack propagation in the coatings, and hence, the cracking behavior is considered in this study

3. EXPERIMENTAL DESIGN AND ANALYSIS

3.1. Center composite design

Response optimization, introduced by Box and Wilson [13], is a very useful tool for designing high-quality products. Center composite design (CCD) is the most popular and appropriate method for quadratic models in RSM [27]. In this study, based on expert experience and reports [1], three factors, namely, laser power, scanning speed, and stand-off distance were studied, while residual stress was the response variable. For each factor, five levels were selected but were coded to the [-2, 2] interval with -2 being the coded lower limit of operating level in the laser cladding and 2 the upper limit to run a CCD. The new level value x_i coded from the natural level X_i was computed as:

$$x_i = 2\left[\frac{2X_i-(X_{max}+X_{min})}{X_{max}-X_{min}}\right] \ , \qquad (2)$$

where X_{max} and X_{min} are the respective natural maximum and minimum level values. In this study, 18 trials including four replicates of the center point and six axial points, were carried out in random order. The factors, along with their natural and coded levels in this study are listed in Table 2. Table 2 shows the experimental conditions and resulting data, which were used for identifying the optimum conditions for laser cladding to obtain the minimum residual stress. Replicates at the center are used to estimate the experimental error.

3.2. Response surface methodology (RSM)

Response surface methodology (RSM) is widely used in the optimization of many types of industrial problems, in the design, development, and formulation of new products, and the improvement of existing product designs. In many cases, first or second order polynomial models are often used in a small response region of interest.

When a linear function is a good fit for the response, a first-order model is used:

$$\hat{y} = \hat{\beta}_0 + \sum_{i=1}^{k}\hat{\beta}_i x_i \ , \qquad (3)$$

and when there is a curvature in the system, the second-order or quadratic model is fitted.

$$\hat{y} = \hat{\beta}_0 + \sum_{i=1}^{k}\hat{\beta}_i x_i + \sum_{i=1}^{k}\hat{\beta}_{ii} x_i^2 + \sum\sum_{i\le j}\hat{\beta}_{ij} x_i x_j \ , \qquad (4)$$

where $\hat{y}$ is the predicted response, $\hat{\beta}_0$, $\hat{\beta}_i$, $\hat{\beta}_{ii}$ and $\hat{\beta}_{ij}$ are the regression parameters to be determined, x_i represents the value of the i^{th} independent variable, and k is the number of independent variables. In this study, the RSM technique is applied to: a – determine the forms of the relationship between the laser factors, such as laser power (X_1), scanning speed (X_2) and stand-off distance (X_3), and the resulting compressive residual stress of clad Y, as well as to: b – optimize the products and the producing procedures. The statistical software package SPSS was employed to analyze the experimental data listed in Table 2.

4. EXPERIMENTAL RESULTS AND DISCUSSION

4.1. Distribution of residual stress

The surface residual stresses computed by x-ray diffraction are only related to the WC-based Co phase on the laser bead surface, as shown in Fig. 2.

Table 2. The center composite design with the original, coded variables and the observed responses

Trials	Natural variables			Coded variables			Compressive stress	
	Laser power	Scanning speed	Stand-off distance	X1	X2	X3	Y	St. dev
	kW	mm/s	mm				MPa	
1	1	4	25	-1	-1	-1	-48.38	6.56
2	2	4	25	1	-1	-1	-50.12	7.96
3	1	8	25	-1	1	-1	-46.81	5.69
4	2	8	25	1	1	-1	-40.32	3.89
5	1	4	45	-1	-1	1	-36.69	3.87
6	2	4	45	1	-1	1	-25.31	2.69
7	1	8	45	-1	1	1	-41.23	6.86
8	2	8	45	1	1	1	-29.47	3.69
9	1.5	6	35	0	0	0	-16.68	2.02
10	1.5	6	35	0	0	0	-20.32	2.96
11	1.5	6	35	0	0	0	-21.65	3.56
12	1.5	6	35	0	0	0	-41.21	5.26
13	0.5	6	35	-2	0	0	-31.51	4.32
14	2.5	6	35	2	0	0	-39.21	4.05
15	1.5	3	35	0	-2	0	-47.36	4.86
16	1.5	9	35	0	2	0	-36.56	3.56
17	1.5	6	20	0	0	-2	-61.71	6.21
18	1.5	6	55	0	0	2	-76.10	7.12

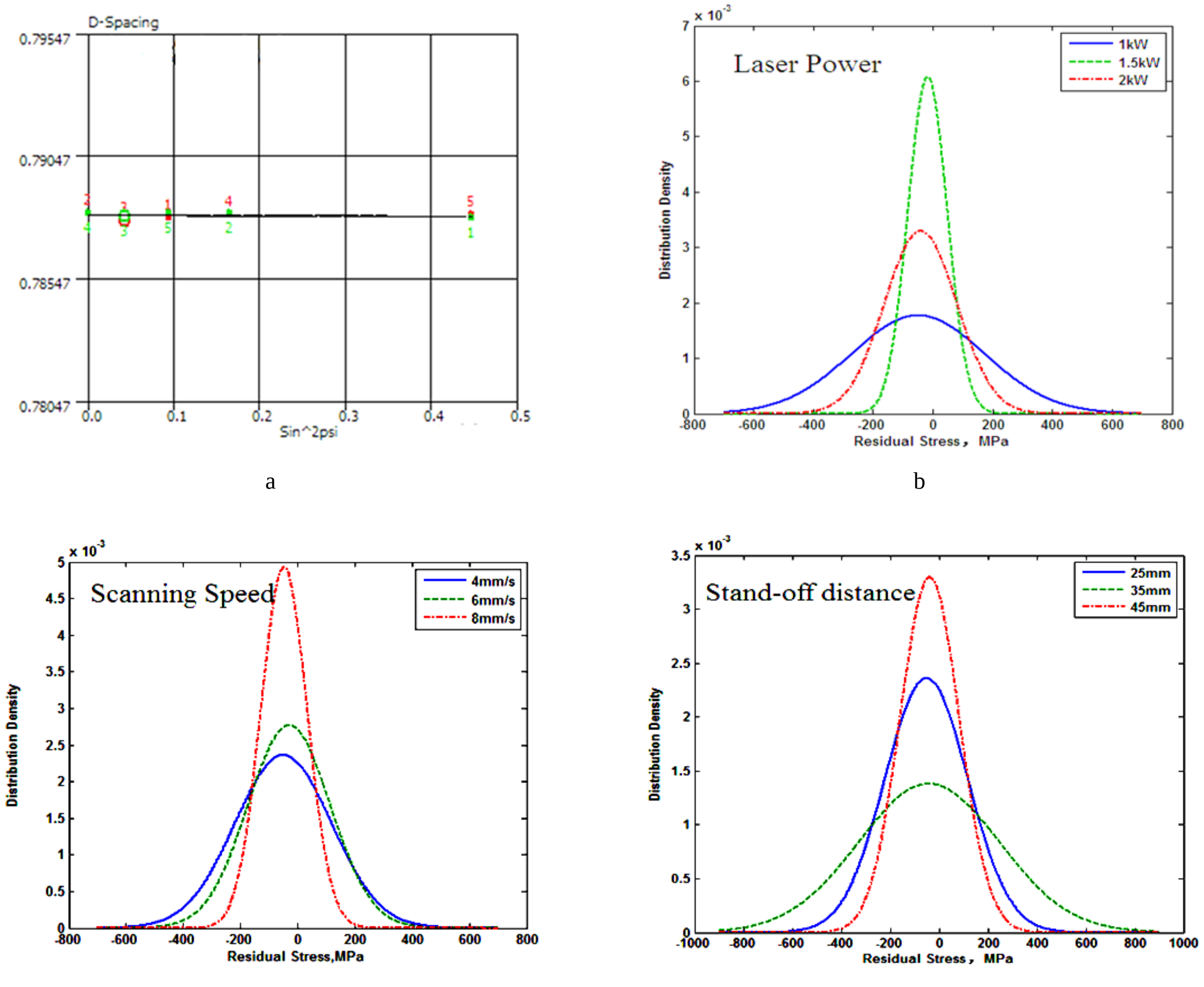

a

b

c

d

Fig. 2. The measured compressive stresses of the pattern of three parameters: a – x-ray diffraction; b – laser power; c – scanning speed; d – stand-off distance

The complete center composite with experimental data is described in Table 2, which presents the compressive value of the residual stress of the clads from the slopes by fitting a Gauss function to an x-ray diffraction peak in Fig. 2 a, in which the strain vs. sin2ψ is plotted using a linear regression function and the residual stress can be determined by the slope corresponding to the compressive residual stresses using Eq. 2. In all cases, the measured residual stresses ranged from -16 MPa to -77 MPa, where they appear to be compressive stresses near the top surface of the laser clads. It is shown that the residual stress distributions on the surface are observed as a smaller fluctuation at the top surface of the clads. Compared with the previous study, the resulting value in the laser clads appeared to be lower when taking into consideration the possible effects of HVOF preset coatings. The distribution of experimental residual stress values of three main parameters including laser power, scanning speed, and stand-off distance, with different conditions are shown in Fig. 2 b and d. The distributions of the three residual stresses during the laser-based HVOF coatings were presented during the overall tests, where the differences between averages and deviations are seen. As shown in Fig. 2 b, the variation and average values of the residual stresses were -43.28 ± 5.36 MPa, -24.97 ± 11.03 MPa, and -36.31 ± 11.17 MPa for laser power of 1.0 kW, 1.5 kW, and 2.0 kW, respectively, indicating low stresses. Compare with Fig. 2 c and d, the residual stress, -16.68 MPa for the laser power of 1.5 kW in trial 9 is significantly improved in the overall tests. This behavior is mainly due to the small grains and more developed secondary dendrites growing in the cladding zone, which can be sufficiently compliant to reduce stress concentration. These features can then sufficiently control the stress propagation to reduce cracking in laser cladding. As shown in Table 2, there is an obvious decrease in the cracking of laser-clad HVOF sprayed with WC-Co coatings with lower residual stress. However, the lower residual stress may not be sufficient to generate the cracks at the melted zone, because both the molten zones are fully melted during laser cladding and a higher thermal gradient is not easily generated in the cladding. Overall, residual stress fields formed inside laser clads and their surroundings in the heat affected zone is far more complicated. Thus, optimal control of residual stress in the laser clads is critical in obtaining high quality mechanical properties in laser cladding without cracking, buckling, or delamination.

4.2. Crack behaviour analysis

For the laser clads of WC/Co-based coating, the macromorphology of the cracks and pores are exhibited in Fig. 3, where a cross section of the sample is etched, and cracks are formed as shown. Compressive residual stress is seen in the laser clads. The large porosities and residual stress-based fractures are observed under optical microscopy, where the visible macropores of the clad are distributed randomly around composite zones in the laser clads. As shown in Fig. 3 a, at residual stress values of -41.23 MPa, several large porosities in the WC/Co clads and partially unmolten particles in the HVOF preset layers were detected, which seemed to appear around the cladded zone, whereas no cracks existed in the unmolten HVOF preset layers. The clads showed excellent metallurgical bonding with the HVOF preset layers. Interestingly, the small cracks generated around the porosity in the WC/Co coating and crack defects between the interlayered areas could not be extended. Further, pores of fully melted composite clads were preferentially induced around the bonding area of the cladded zones, as shown in Fig. 3b, at a residual stress value of -39.21 MPa. Compared with other cladded samples without fully melted preset layers, the pores of the completely melted cladded zone were much larger. The cross-sectional morphology of the pores indicates that most of the pores occurred at the bonding interface and the cracking cannot be seen. As seen in Fig. 3 c, at residual stress of -76.10 MPa, a high concentration of stress occurs near the melted regions, and cracks were created in the laser-welded region. In addition, the crack propagation path did not grow around most of the porous area in the melted zone. As illustrated in Fig. 3 d, at a residual stress of -61.71 MPa, cracks were produced in the unmolten HVOF zone and the upper part of the heat affected zone, micro-pores were observed near the HVOF regions, and a visible difference could be observed in the crack propagation type. However, in laser clads with HVOF preset layers, the majority of cracks were on the unmolten HVOF interface and in the zone of the laser clads. All cracks in the HVOF preset layers extended to the heat affected zone, while they were produced frequently at the cladded bonding zone. The origin of the crack was closely examined using SEM micrographs of crack fracture, as shown in Fig. 3 e.

Small cracks were preferentially initiated and propagated from the fractured porosities in Trial 15 at -59.2 MPa residual stress, where porosities associated with micro-cracks were induced within the HVOF preset layer. This indicates that the porosity initiation sites into a laminar structure easily created the cracks at high stress concentrations, as the HVOF forms a lamellar structure with many unmolten particles and pores. As shown in Fig. 3 f, at residual stress of -16.68 MPa, the microstructures of the cladded zone mainly consist of fine dendritic structures due to rapid solidification. Small grains and more developed secondary dendrites could be grown in the cladded zone. Several micro-cracks along with eutectic phases in the dendrites were formed during the cladded area. However, highly developed dendrites have several nano crack-like features when minor stresses appear under the laser clads, suggesting these features can be compliant enough to reduce the stress in laser clads.

Based on Fig. 3 and Table 3, the cracking susceptibility of laser clads with HVOF WC/CO coatings may be attributed to the high content of carbides, pores and the brittle eutectic phases. The thermally induced residual stresses during the cladding process are the main driving forces in crack propagation. It seems reasonable to conclude that residual stress experiments are important to understand crack growth in laser-based HVOF coatings.

4.3. Microstructure of laser-based HVOF clads

Fig. 4 shows the metallographic observation along with the cross-section of the coating revealing the features of the different zones including a laser cladded zone, bonding zone, remelted zone (HVOF), and heat affected zone in microcracks in all the samples. As shown in Fig. 4 a, the vicinity of the HVOF zones show white splats with a characteristically brighter unmolten zone that was free from microcracks. Several pores in laser clads were still seen, but the good bonding between the WC/Co and HVOF coatings and carbide inclusions in the HVOF coatings using the diffusion mechanism were clear in the laser clads. In contrast, the laser clads in Fig. 4 b formed a fully melted zone around the HVOF coatings in the laser clads, where the laser-clad layers were distributed uniformly. In other words, the unmolten particles almost disappeared when the laser power was increased to 1.5 kW, but some large pores appeared near the top coating surface. In addition, the metallurgical bond could be recognized in the laser clads. As a result, this can enhance the composite effect of the plasma and the laser beam. A magnified image of the partial by melted region is provided in Fig. 4 c, where a cross-sectional SEM micrograph taken from a shallow part in the bonding zone is shown. It can be found the microstructure of the right-side white area was unmolten during HVOF coatings, but the left area with dendrites and eutectic phases was melted near the interface due to a higher temperature gradient from the coating/substrate interface. As shown in Fig. 4 d, more energy entered into the HVOF-sprayed coatings because of the enhanced laser power and high heat that fully melted in the HVOF- sprayed coating layers flowing out of the cladding layer towards the substrate.

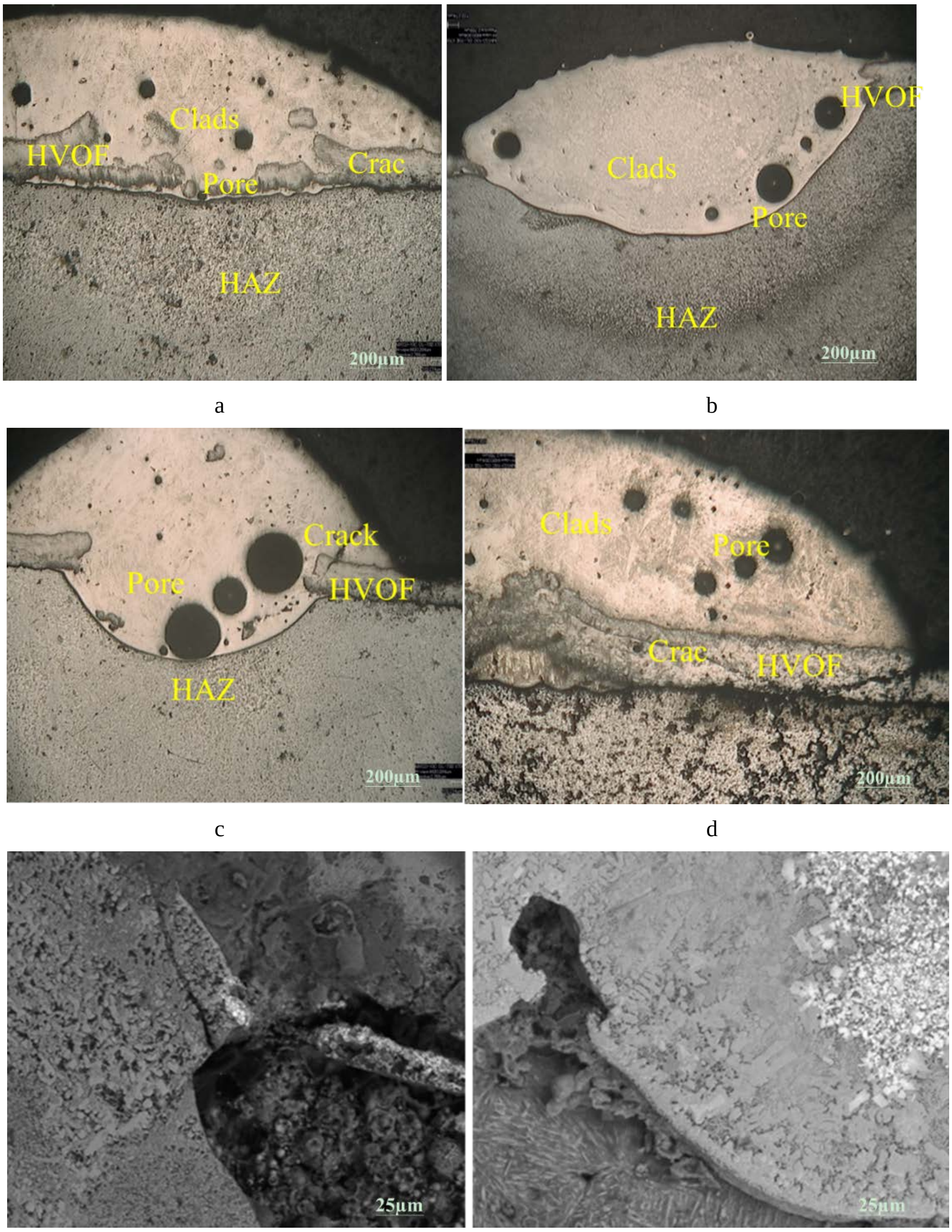

a b

c d

e f

Fig. 3. Optical macro-crack features of laser cladded zone: a – trial 7 of -41.23 MPa; b – trial 14 of -39.21 MPa; c – trial18 of -76.10 MPa; d – trial17 of -61.71 MPa, magnified 500X SEM; e – trial15 of -59.20 MPa; f – trial 9 of -16.68 MPa

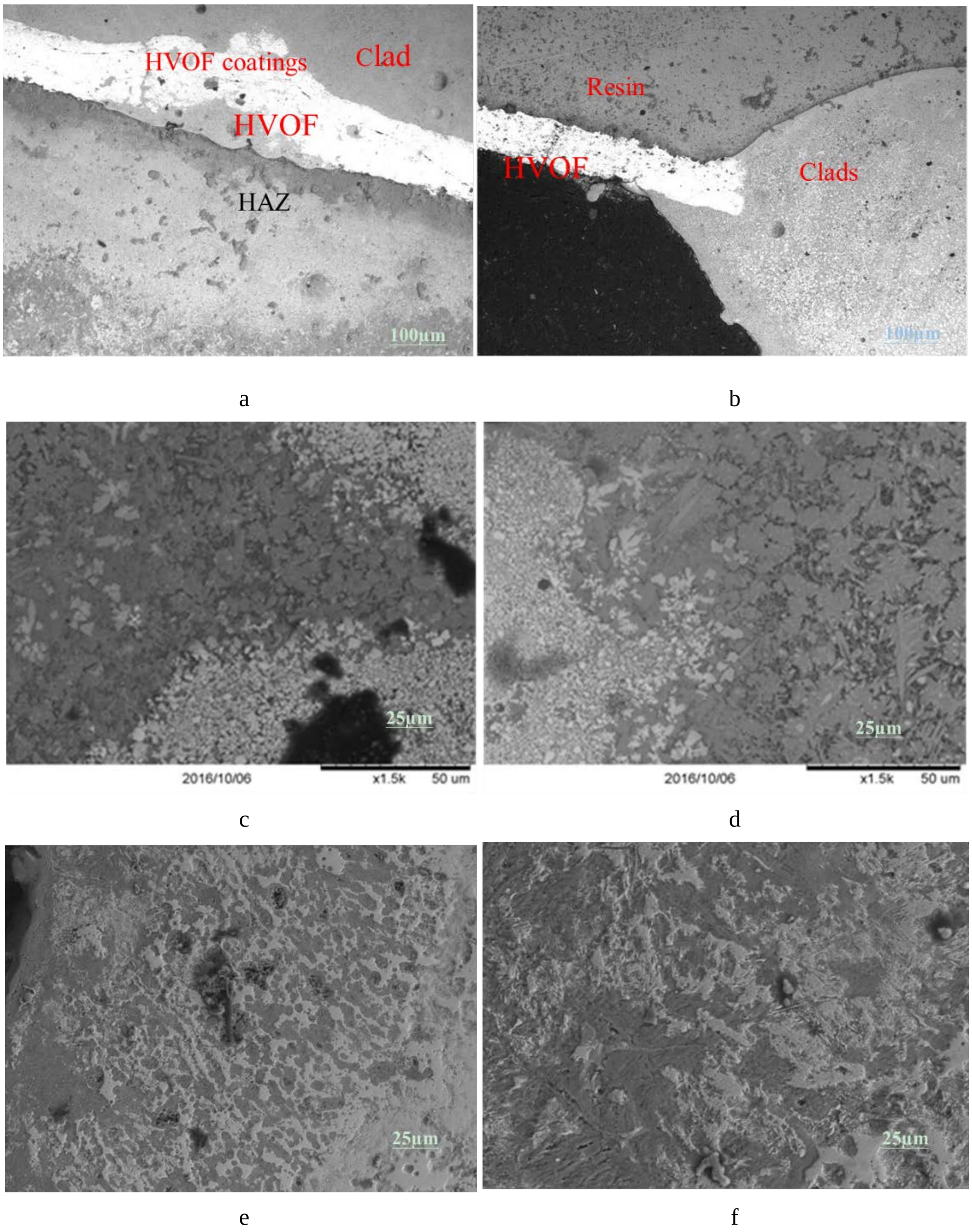

a b c d e f

Fig. 4. SEM morphologies of the cross-sections of WC/Co cladding layer with a cladding area and heat affected zone of HVOF coatings at different laser powers: a – brighter image with no melted zone; b – brighter image with partial melted region; c – magnified image of the partially melted region; d – magnified image of the melted region; e – HAZ region; f – near matrix region

This led to a complete fusion and recrystallization process between the bonding zones, and the dendrites being more columnar and vertical through the interface around the bonding zone. Comparatively, the microstructure of the bonding region differs totally from that of the cladding layer. This is due to the inter-diffusion of alloying elements as well as the additional intermetallic phases formed during laser cladding. In the HAZ shown in Fig. 4 e, the substrate material was perfectly reheated despite the HVOF- sprayed coatings being coarsened.

In the HAZ shown in Fig. 4 e, the substrate material was perfectly reheated despite the HVOF-sprayed coatings being coarsened. As seen in Fig. 4 e, the laser cladding of the HVOF-sprayed coating yielded a smoother, pore free coating with a cross-section, which had finer dendritic structures only in the heat-affected area of the substrate. In addition, in the HAZ of the substrate, the unmolten particles and porosity in the coatings decreased at 1.5 kW laser power. The structure of the coatings was dense, and a dendritic structure was formed due to the rapid cooling rate of laser processing, as shown in Fig. 4 f. A tiny dendritic region in the HAZ is depicted in Fig. 2 f as compared to Fig. 4 e. Clearly, the bead demonstrated in the laser cladding showed a comparatively uniform distribution of crystallographic texture compared to the beads of the HVOF-sprayed coatings. In other words, the laser clads were completely melted with the removal of the porosity and splat boundaries, as well as the formation of a metallurgical bonding mechanism, where a homogeneous microstructure was present in all the molten zones and the HVOF-sprayed coating had lamellar grains with mechanical interlocking bonds and defects. It can be concluded that laser clads with highly dense structures could improve the performance of these hard coatings deposited by HVOF techniques.

4.4. Building empirical models of quadratic responses

Table 3 and Table 4 present the results from the analysis of variance (ANOVA) and the model-fitting procedures based on three different models incorporating linear, first-order pairwise interactions, and quadratic polynomial equations. From Table 3, the F-statistics for testing the significance of the linear, interaction, and quadratic models are 0.069, 0.078 and 8.876, respectively, with the respective p-values of 0.975, 0.997, and 0.0027. A model with a p-value < 0.05 indicates that the model is significant and appropriate for fitting the data. Based on the small p-values for the quadratic terms, the second-order model is found to be adequate for fitting the responses. In addition, the analysis in Table 3 shows that the quadratic terms contribute significantly to the model and an R^2 of 0.909 indicates a good fit between the experimental data and predicted values. Further, from Table 4, we conclude that the y-intercept, both first- and second-order of both scanning speed (X_2), and stand-off distance (X_3) on the laser clads are statistically significant with p-values < 0.05, while the laser power (X_1), all the pairwise interactions X_1X_2, X_2X_3, X_1X_3, and the quadric X_1^2 are not significant. Thus, including quadratic terms would be more accurate for predicting the responses as compared with those in the first-order and interaction model. The fitted quadratic regression model of compressive stress for the laser cladded region, based on the regression analysis, is

$$Y = -96.247 + 17.496X_1 + 18.105X_2 + 11.247X_3 + 1.076X_1X_2 - 0.125X_2X_3 + 0.460X_1X_3 - 12.828X_1^2 - 1.214X_2^2 - 0.152X_3^2. \quad (5)$$

4.5. Predictive analysis for the quadratic model

A graph of the actual data versus the predictive values is shown in Fig. 5, which can be used to detect an accurate response pattern. The red line represents the predicted response from the quadratic model, and the two black lines cover the ranges of ± one standard deviation of the mean. As can be readily seen, most of the predictions from the quadratic model are within one standard deviation of the average, except for the sixth and fourteenth trials. This indicates that the quadratic model provides a good prediction. In addition, the predictive results with a first-order, pair-order, and second-order function in the overall trials may be compared in Fig. 6. The quadratic model is lower in predictive error. A significant difference exists between the statistical errors based on the predictions obtained from these models.

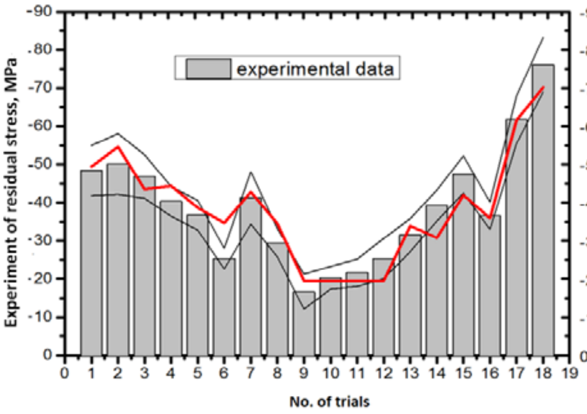

Fig. 5. The observed and predicted residual stresses from the quadratic model

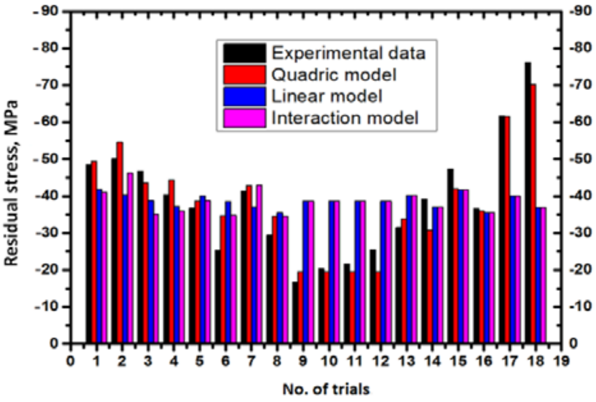

Fig. 6. Comparisons of the observed and predicted residual stresses from linear, interaction and quadratic models

Table 3. Results of analysis of variance for response fitting with linear, interaction and quadratic models

Source	Sum of squares	Degrees of freedom	Mean squares	F-value	p-value	R^2
Linear	57.715	3	19.238	0.069	0.975	0.0147
Interaction	159.599	6	26.600	0.078	0.997	0.4047
Quadrate	3561.658	9	395.740	8.876	0.0027	0.9089

Table 4. Estimations based on the quadratic model

Source	Coefficient estimate	Standard error	t-statistical	P-value
Intercept	-296.247	53.648	5.522	0.001
$X1$	17.496	27.814	-0.629	0.547
$X2$	18.105	6.954	-2.604	0.031
$X3$	11.247	1.635	-6.877	0.000
X_1X_2	1.076	2.361	-0.456	0.661
X_2X_3	-0.125	0.118	1.062	0.319
X_3X_1	0.460	0.472	-0.974	0.359
X_1^2	-12.828	5.664	2.265	0.053
X_2^2	-1.214	0.354	3.430	0.009
X_3^2	-0.152	0.018	8.667	0.000

4.6. Influences of laser cladding parameters on residual stresses

The main objective of this study was to determine a set of laser operating conditions that would achieve the minimum residual stress in the clads. The graphical analysis for the quadratic model in Eq. 4 was made from the contour plots of the predicted response, where the optimization of laser operating conditions is determined. As shown in Fig. 7 – Fig. 9, the stationary points are obtained through the individual partial derivatives in Eq. 4 to identify the minimal responses. In other words, the optimal levels of X_1, X_2, and X_3 for the predicted response are derived from the partial derivatives.

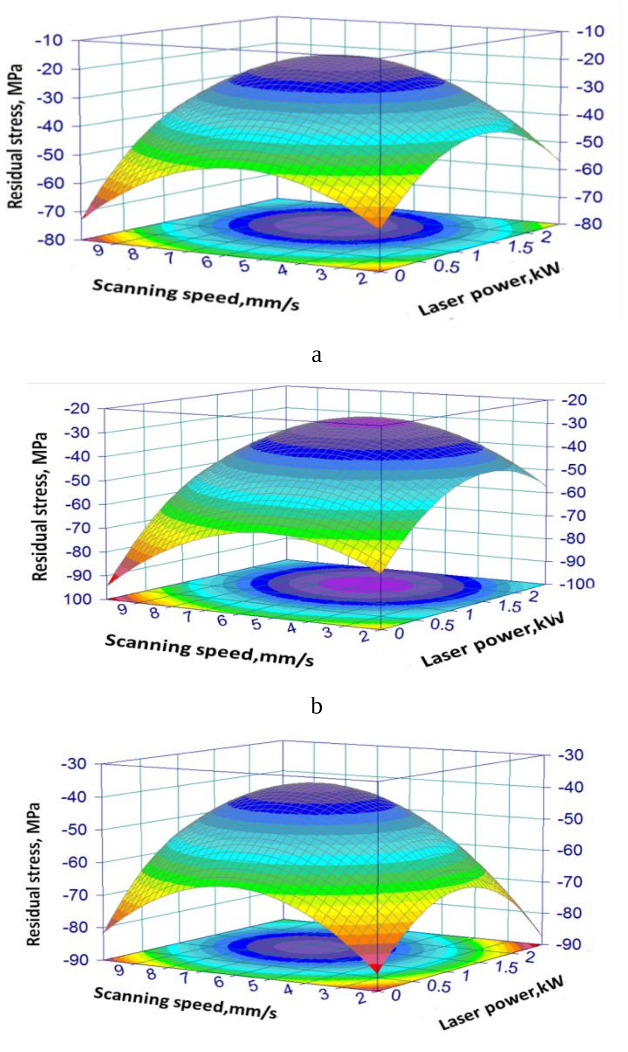

a

b

c

Fig. 7. Contour plots from the quadratic response surface for laser power and scanning speed at fixed stand-off distance: a – 25 mm; b – 35 mm; c – 45 mm

In addition, Fig. 7 – Fig. 9 show the three-dimensional response surfaces and contour plots for the yield response predicted from the quadratic model for two factors while holding the third factor constant at three different values. The response surface with the contour plots shown in Fig. 7 shows the responses from various laser power and scanning speed at fixed stand-off distances of 25 mm, 35 mm, and 45 mm, respectively.

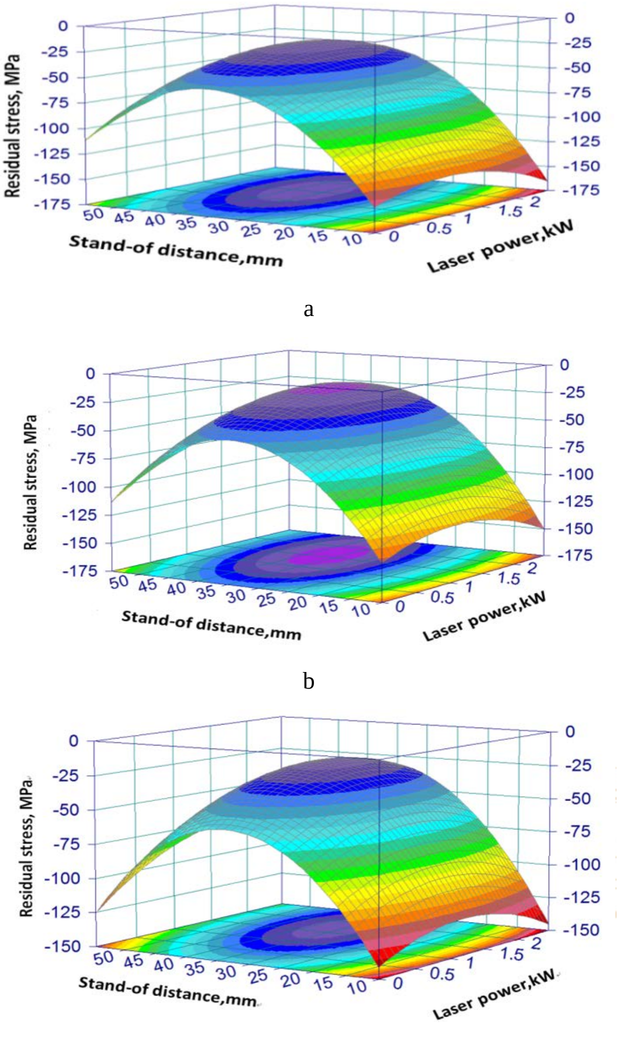

a

b

c

Fig. 8. Contour plots from the quadratic response surface for laser power and stand-off distance at fixed scanning speed: a – 4 mm/s; b – 6 mm/s; c – 8 mm/s

The response plot displayed lower residual stresses at medium laser power and increased at a higher or lower scanning speed. Fig. 8 and Fig. 9 show similar results. However, it can be seen that residual stress depends more on the stand-off distance than on the laser power. That is, low residual stresses are obtained at a medium stand-off distance using the medium laser power. Furthermore, from closer examinations in Fig. 7 – Fig. 9 and comparisons, the minimum residual stress of -18.91 MPa is achieved in Fig. 9 b at 1.5 kW laser power, where the projected circle on the plain is centered at the scanning speed at 6 mm/s and stand-off distance at 35 mm as the stationary point. This result was consistent with the actual observed responses from the experiments.

5. CONCLUSIONS

The use of a response surface methodology was experimentally validated with a center composite design being an effective and efficient way to optimize the production of high efficiency, high quality laser cladding coatings. Using laser power, scanning speed and stand-off distance as the three factors, minimization of residual stresses yielded from the laser clads of HVOF coatings was achieved. The following conclusions were drawn:

1. Typically, the measured residual stresses appeared to be compressive on the top surface of the laser clads. The laser clads tend to stretch as the shots affect the top surface of the HVOF coatings but are restrained by the HVOF coating layer. Cracking of the laser clads is barely induced in this area. The clad layer and the associated heat affected zone in the laser clads at a highly compressive residual stress are clearly evident, and the crack of the clad is propagated randomly around these zones in laser clads.

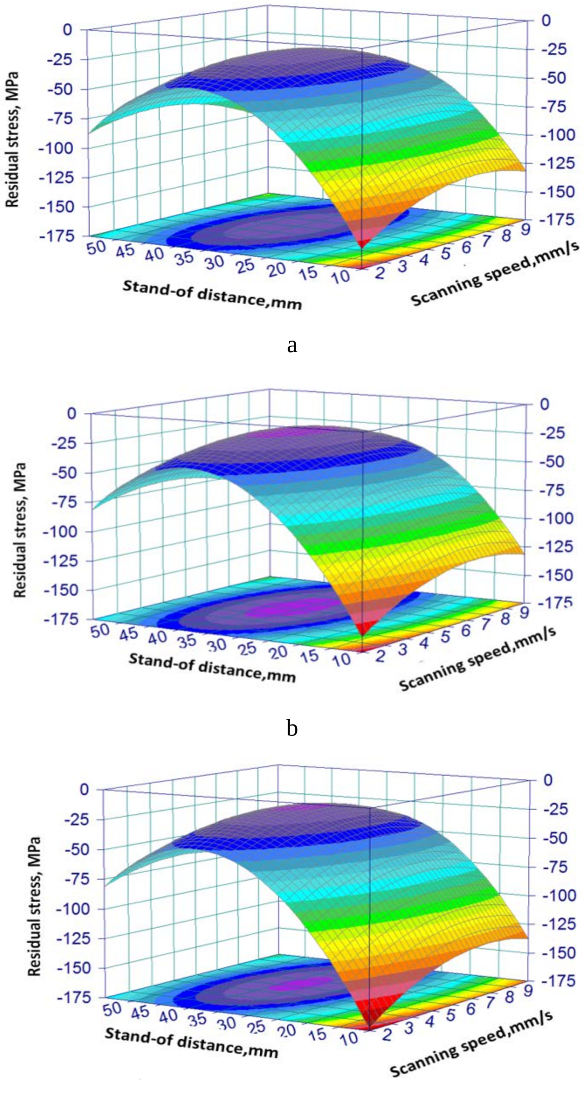

a

b

c

Fig. 9. Contour plots from the quadratic response surface for scanning speed and stand-off distance at a fixed laser power: a – 1 kW; b – 1.5 kW; c – 2.5 kW

2. The laser clads were completely melted with the removal of porosity and splat boundaries, as well as the formation of a metallurgical bonding mechanism. A fine microstructure was observed in the molten zones while the HVOF-sprayed coating had lamellar grains with mechanical interlocking bonds and defects. It can be concluded that laser clads with highly dense structures could improve the unmolten properties of these deposited by HVOF.
3. The predictive results using a first-order, pairwise, and second-order function in all the trials were compared. The second-order model has a lower percentage of predictive error values that exceed 10 percent. The second-order function is remarkably more precise for predictive values compared to terms in the linear or pairwise interaction model.

Acknowledgements

This work was financially supported by the Project of Fujian Federation of Social Sciences (FJ2021B177).

REFERENCES

1. **Suryanarayanan, R.** Plasma Spraying: Theory and Applications. *World Scientific.* 1993: p. 308. https://doi.org/10.1142/1994
2. **Babu, P.S., Basu, B., Sundararajan, G.** Processing–Structure–Property Correlation and Decarburization Phenomenon in Detonation Sprayed WC–12Co Coatings *Acta Materialia* 56 (18) 2008: pp. 5012 – 5026. https://doi.org/10.1016/j.actamat.2008.06.023
3. **Guilemany, J.M., Dosta, S., Nin, J., Miguel, J.R.** Study of the Properties of WC-Co Nanostructured Coatings Sprayed by High-Velocity Oxyfuel *Journal of Thermal Spray Technology* 14 (3) 2005: pp. 405 – 413. https://doi.org/10.1361/105996305X59350
4. **Shipway, P.H., Mccartney, D.G., Sudaprasert, T.** Sliding Wear Behaviour of Conventional and Nanostructured HVOF Sprayed WC–Co Coatings *Wear* 259 (7 – 12) 2005: pp. 820 – 827. https://doi.org/10.1016 j. wear. 2005.02.059
5. **Krishna, B.V., Misra, V.N., Mukherjee, P.S., Sharma, P.** Microstructure and Properties of Flame Sprayed Tungsten Carbide Coatings *International Journal of Refractory Metals & Hard Materials* 20 (5 – 6) 2002: pp. 355 – 374. https://doi.org/10.1016/S0263-4368(02)00073-2
6. **Guilemany, J.M., Dosta, S., Miguel, J.R.** The Enhancement of the Properties of WC-Co HVOF Coatings Through the Use of Nanostructured and Microstructured Feedstock Powders *Surface & Coatings Technology* 201 (3) 2006: pp. 1180 – 1190. https://doi.org/10.1016/j.surfcoat.2006.01.041
7. **Jin, K., Kuroda, S., Kodama, T.** Evaluation of Through-Porosity of HVOF Sprayed Coating *Surface & Coatings Technology* 166 (1) 2003: pp. 17 – 23. https://doi.org/10.1016/S0257-8972(02)00719-3
8. **Zhu, Y.C., Ding, C.X., Yukimura, K., Xiao, T.D., Strutt, P.R.** Deposition and Characterization of Nanostructured WC–Co Coating *Ceramics International* 27 (6) 2001: pp. 669 – 674. https://doi.org/10.1016/S0272-8842(01)00016-5
9. **Barbera-Sosa, J.G.L., Santana, Y.Y., Staia, M.H., Chicot, D., Lesage, J., Caro, J., Mesmacque, G., Puchi-Cabrera, E.S.** Microstructural and Mechanical Characterization of Ni-Base Thermal Spray Coatings Deposited by HVOF *Surface & Coatings Technology* 202 (18) 2008: pp. 4552 – 4559. https://doi.org/10.1016/j.surfcoat.2008.04.041
10. **Cho, T.Y., Yoon, J.H., Kim, K.S., Song, K.O., Joo, Y.K., Fang, W., Zhang, S.H., Youn, S.J., Chun, H.G., Hwang, S.Y.** A Study on HVOF Coatings of Micron and Nano WC–Co Powders *Surface & Coatings Technology*

202 (22 – 23) 2008: pp. 5556 – 5559. https://doi.org/10.1016/j.surfcoat.2008.06.106

11. **Huang, Y., Zeng, X.** Investigation on Cracking Behavior of Ni-Based Coating by Laser-Induction Hybrid Cladding *Applied Surface Science* 256 (20) 2010: pp. 5985 – 5992. https://doi.org/10.1016/j.apsusc.2010.03.106
12. **Oliveira, U.D., Ocelík, V., Hosson, J.T.M.D.** Residual Stress Analysis in Co-Based Laser Clad Layers by Laboratory X-rays and Synchrotron Diffraction Techniques *Surface & Coatings Technology* 201 (3 – 4) 2006: pp. 533 – 542. https://doi.org/10.1016/j.surfcoat.2005.12.011
13. **Sun, G., Zhou, R., Lu, J., Mazumder, J.** Evaluation of Defect Density, Microstructure, Residual Stress, Elastic Modulus, Hardness and Strength of Laser-Deposited AISI 4340 Steel *Acta Materialia* 84 (84) 2015: pp. 172 – 189. https://doi.org/10.1016/j.actamat.2014.09.028
14. **Afzal, M., Ajmal, M., Khan, A.N., Hussain, A., Akhter, R.** Surface Modification of Air Plasma Spraying WC–12%CO Cermet Coating by Laser Melting Technique *Optics & Laser Technology* 56 (1) 2014: pp. 202 – 206. https://doi.org/10.1016/j.optlastec.2013.08.017
15. **Qian, J., Yin, Y., Li, T.J., Hu, X.T., Wang, C., Li, S.Q.** Structure, Micro-Hardness and Corrosion Behaviour of the AL–SI/AL$_2$O$_3$, Coatings Prepared by Laser Plasma Hybrid Spraying on Magnesium Alloy *Vacuum* 117 2015: pp. 55 – 59. https://doi.org/10.1016/j.vacuum.2015.04.005
16. **Wen, P., Feng, Z., Zheng, S.** Formation Quality Optimization of Laser Hot Wire Cladding for Repairing Martensite Precipitation Hardening Stainless Steel *Optics & Laser Technology* 65 2015: pp. 180 – 188. https://doi.org/10.1016/j.optlastec.2014.07.017
17. **Sun, Y., Hao, M.** Statistical Analysis and Optimization of Process Parameters in TI6AL4V Laser Cladding Using Nd:YAG Laser *Optics & Lasers in Engineering* 50 (7) 2012: pp. 985 – 995. https://doi.org/10.1016/j. optlaseng. 2012.01.018
18. **Farahmand, P., Kovacevic, R.** Laser Cladding Assisted with an Induction Heater (LCAIH) of NI–60%WC Coating *Journal of Materials Processing Technology* 222 2015: pp. 244 – 258. https://doi.org/10.1016/j.jmatprotec.2015.02.026
19. **Afzal, M., Khan, A.N., Mahmud, T.B., Khan, T.I., Ajmal, M.** Effect of Laser Melting on Plasma Sprayed WC-12 wt.%Co Coatings *Surface & Coatings Technology* 266 2015: pp. 22 – 30. https://doi.org/10.1016/j.surfcoat.2015.02.004
20. **Rakhes, M., Koroleva, E., Liu, Z.** Improvement of Corrosion Performance of HVOF MMC Coatings by Laser Surface Treatment *Proceedings of the 36th International MATADOR Conference,* Springer London. 2010: pp. 729 – 733. https://doi.org/10.1007/978-1-84996-432-6_117
21. **Luo, Q., Jones, A.H.** High-precision Determination of Residual Stress of Polycrystalline Coatings Using Optimised XRD-sin 2 ψ Technique *Surface & Coatings Technology* 205 (5) 2010: pp. 1403 – 1408. https://doi.org/10.1016/j.surfcoat.2010.07.108
22. **Luo, W., Selvadurai, U., Tillmann, W.** Effect of Residual Stress on the Wear Resistance of Thermal Spray Coatings *Journal of Thermal Spray Technology* 25 (1) 2016: pp. 321 – 330. https://doi.org/10.1007/s11666-015-0309-0
23. **Zoei, M.S., Sadeghi, M.H., Salehi, M.** Effect of Grinding Parameters on the Wear Resistance and Residual Stress of HVOF-deposited WC-10Co-4Cr coating *Surface & Coatings Technology* 307 2016: pp. 886 – 891. https://doi.org/10.1016/j.surfcoat.2016.09.067
24. **Guilemany, J.M., Dosta, S., Miguel, J.R.** The Enhancement of the Properties of WC-Co HVOF Coatings Through the Use of Nanostructured and Microstructured Feedstock Powders *Surface & Coatings Technology* 201 (3) 2006: pp. 1180 – 1190. https://doi.org/10.1016/j.surfcoat.2006.01.041
25. **Myers, R.H., Montgomery, D.C., Anderson-Cook, C.M.** Response Surface Methodology: Process and Product Optimization Using Designed Experiments. 3rd ed, John Wiley & Sons, Inc., Hoboken, New Jersey. 2009.
26. **Lin, B.T., Jean, M.D., Chou, J.H.** Using Response Surface Methodology for Optimizing Deposited Partially Stabilized Zirconia in Plasma Spraying *Applied Surface Science* 253 (6) 2007: pp. 3254 – 3262. https://doi.org/10.1016/j.apsusc.2006.07.021
27. **Kapadia, P., Davies, C., Pirling, T., Hofmann, M., Wimpory, R., Hosseinzadeh, F., Dean, D., Nikbin, K.** Quantification of Residual Stresses in Electron Beam Welded Fracture Mechanics Specimens *International Journal of Solids & Structures* 106 – 107 2017: pp. 106 – 118. https://doi.org/10.1016/j.ijsolstr.2016.11.028
28. **Stadelmann, R., Lugovy, M., Orlovskaya, N., Mchaffey, P., Radovic, M., Sglavo, V.M., Grasso, S., Reece, M.J.** Mechanical Properties and Residual Stresses in Zrb2–Sic Spark Plasma Sintered Ceramic Composites *Journal of the European Ceramic Society* 36 (7) 2016: pp. 1527 – 1537. https://doi.org/10.1016/j.jeurceramsoc.2016.01.009
29. **Zafar, S., Sharma, A.K.** Investigations on Flexural Performance and Residual Stresses in Nanometric WC-12Co Microwave Clads *Surface & Coatings Technology* 291 2016: pp. 413 – 422. https://doi.org/10.1016/j.surfcoat.2016.03.009
30. **Wang, C., Jiang, C., Ji, V.** Thermal Stability of Residual Stresses and Work Hardening of Shot Peened Tungsten Cemented Carbide *Journal of Materials Processing Technology* 240 2016: pp. 98 – 103. https://doi.org/10.1016/j.jmatprotec.2016.09.013
31. **Suárez, A., Amado, J.M., Tobar, M.J., Yáñez, A., Fraga, E., Peel, M.J.** Study of Residual Stresses Generated Inside Laser Cladded Plates Using Fem and Diffraction of Synchrotron Radiation *Surface & Coatings Technology* 204 (12 – 13) 2010: pp. 1983 – 1988. https://doi.org/10.1016/j.surfcoat.2009.11.037
32. **Pan, R., Kovacevic, S., Lina, T., He, P., Sekulic, D.P., Mesarovic, S.Dj., Yang, Z.H., Shen, Y.X., Wei, H.** Control of Residual Stresses in 2Si-B-3C-N and Nb Joints by the Ag-Cu-Ti + Mo Composite Interlayer *Materials & Design* 99 2016: pp. 193 – 200. https://doi.org/10.1016/j.matdes.2016.03.072
33. **Walker, T.R., Bennett, C.J., Lee, T.L., Clare, A.T.** A Novel Numerical Method to Predict the Transient Track Geometry and Thermomechanical Effects through In-situ Modification of the Process Parameters in Direct Energy Deposition *Finite Elements in Analysis and Design* 169 2020: pp. 103347 (1 – 20). https://doi.org/10.1016/j.finel.2019.103347
34. **Kovalev, O.B., Bedenko, D.V., Zaitsev, A.V.** Development and Application of Laser Cladding Modeling Technique: From Coaxial Powder Feeding to Surface Deposition and

Bead Formation *Applied Mathematical Modelling* 57 2018: pp. 339 – 359. https://doi.org/10.1016/ j.apm.2017.09.043

35. **Liu, C.W., Jean, M.D., Wang, Q.T., Chen, B.S.** Optimization of Residual Stresses in Laser-Mixed WC(Co, Ni) Coatings *Strength of Materials* 51 (1) 2019: pp. 95 – 101. https://doi.org/10.1007/s11223-019-00054-z
36. **Jean, M.D., Lei, P.D., Kong, L.H., Liu, C.W.** Aluminum Nitride Coatings Using Response Surface Methodology to Optimize the Thermal Dissipated Performance of Light-Emitting Diode Modules *AIP Advances* 8 2018: pp. 055106. https://doi.org/10.1063/1.5021816